Comprehensive Comparison of Image Quality Aspects Between Conventional and Plane-Wave Imaging Methods on a Commercial Scanner

Gijs A. G. M. Hendriks, *Member, IEEE*, Gert Weijers, Chuan Chen, *Student Member, IEEE*, Madeleine Hertel, *Student Member, IEEE*, Chi-Yin Lee, *Senior Member, IEEE*, Peter M. Dueppenbecker, Marcus Radicke, Andy Milkowski, Hendrik H. G. Hansen, and Chris L. de Korte, *Senior Member, IEEE*

***Abstract*— Coherent plane-wave compound imaging (CPWCI) is used as alternative for conventional focused imaging (CFI) to increase frame rates linearly with the ratio number of imaging lines to steering angles. In this study, the image quality was compared between CPWCI and CFI, and the effect of steering angles (range and number) and beamforming strategies was evaluated in CPWCI. In automated breast volume scanners (ABVSs), which suffer from reduced volume rates, CPWCI might be an excellent candidate to replace CFI. Therefore, the image quality of CFI currently in ABVS and CPWCI was also compared in an *in vivo* breast lesion. Images were obtained by a Siemens Sequoia ultrasound system, and two transducers (14L5 and 10L4) in a CIRS multipurpose phantom (040GSE) and a breast lesion. Phantom results showed that contrast sensitivity and resolution, axial resolution, and generalized contrast-to-noise ratio (gCNR; imaging depths $<$45 mm) were similar for most imaging sequences. CNR (imaging depths $\geq$45 mm), penetration, and lateral resolution were significantly improved for CPWCI (15 angles) compared to CFI for both transducers. In CPWCI, certain combinations of steering angles and beamforming methods yielded improved gCNR (small angles and delay-and-sum) or lateral resolution (large angles and Lu's-fk). Image quality seemed similar between CPWCI and CFI (three angles incoherent compounded as in ABVS) by visual inspection of the *in vivo* breast lesion images.**

***Index Terms*— Beamformer, breast imaging, coherent compounding, conventional imaging, delay-and-sum (DAS), plane-wave imaging (PWI), ultrasound (US) imaging.**

Manuscript received March 16, 2022; accepted March 31, 2022. Date of publication April 11, 2022; date of current version May 26, 2022. This work was supported by Siemens Healthineers GmbH, Forchheim, Germany. *(Corresponding author: Gijs A. G. M. Hendriks.)*

This work involved human subjects or animals in its research. Approval of all ethical and experimental procedures and protocols was granted by the CMO Radboudumc, Nijmegen, The Netherlands under Application No. 2021-7421, and performed in line with the Declaration of Helsinki (version 9th Juli 2018).

Gijs A. G. M. Hendriks, Gert Weijers, Chuan Chen, and Hendrik H. G. Hansen are with the Medical UltraSound Imaging Center, Department of Medical Imaging, Radboud Institute for Health Sciences, Radboud University Medical Center, 6500 HB Nijmegen, The Netherlands (e-mail: gijs.hendriks@radboudumc.nl).

Madeleine Hertel, Peter M. Dueppenbecker, and Marcus Radicke are with Siemens Healthcare GmbH, 91301 Forchheim, Germany.

Chi-Yin Lee and Andy Milkowski are with Siemens Medical Solutions USA, Inc., Issaquah, WA 98029 USA.

Chris L. de Korte is with the Medical UltraSound Imaging Center, Department of Medical Imaging, Radboud Institute for Health Sciences, Radboud University Medical Center, 6500 HB Nijmegen, The Netherlands, and also with the Physics of Fluids Group, MIRA, University of Twente, 7500 AE, Enschede, The Netherlands.

This article has supplementary downloadable material available at https://doi.org/10.1109/TUFFC.2022.3165632, provided by the authors.

Digital Object Identifier 10.1109/TUFFC.2022.3165632

I. Introduction

PLANE-WAVE imaging (PWI) is an ultrasound (US) imaging technique [1], [2] to increase the frame rate compared to conventional focused imaging (CFI) and can be used in B-mode imaging and functional applications (e.g., elastography, flow and Doppler imaging). In CFI [Fig. 1(a)], the transducer transmits narrow-focused US beams and receives backscattered US signals per beam. This acquisition scheme is repeated such that an image can be reconstructed line-by-line. In PWI [Fig. 1(b)], an array of elements transmits simultaneously, forms an unfocused US beam, and receives backscattered US signals per element. Next, the element data are focused in receive to form image data by various beamforming algorithms such as delay-and-sum (DAS) in the temporal–spatial domain, and Lu's-fk [3], [4] and Stolt's-fk [5] in the Fourier domain. Both Fourier-based methods benefit from a reduced computational cost compared to adaptive beamformers and commonly used DAS. Lu's-fk and Stolt's-fk regard the received signals as integral and transform the wavenumber via Fourier spectrum migration. The difference between Lu's-fk and Stolt's-fk mainly lies in the spectrum migration relation for the large lateral wavenumber.

In PWI, multiple image lines are obtained simultaneously by a single transmit–receive event, whereas image lines are obtained line-by-line in CFI. Therefore, the frame rate in PWI theoretically can be increased with the number of imaging lines obtained in CFI. However, the increased frame rate comes at cost of reduced image quality due to unfocused

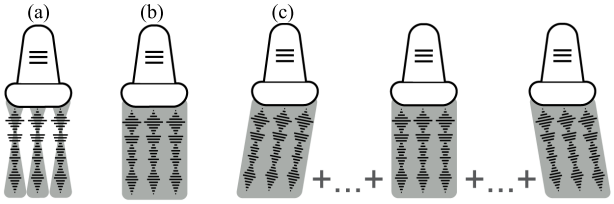

Fig. 1. Schematic visualization of the recording of three US lines (~192 in reality and insonified area in gray) by (a) CFI, (b) PWI, and (c) CPWCI in which US data of multiple steering angles are coherently compounded.

transmissions. To overcome this limitation, coherent plane-wave compound imaging (CPWCI) was introduced in which reconstructed US data of multiple steering angles are coherently compounded to increase image quality in Fig. 1(d), see [6], [7]. Compared to CFI, the frame rate in CPWCI increases with the number of required imaging lines divided by the number of required steering angles.

Some studies evaluated and compared the image quality of CPWCI and CFI [6], [8], and however, only a limited number of image quality parameters and settings were investigated on a US research system instead of a clinical high-end system used in practice. Contrast and lateral resolution were often only evaluated. According to Thijssen *et al.* [9] and the European guidelines for quality assurance in US [10], image quality should be evaluated in terms of axial (Ax) and lateral (Lat) resolution (Res), penetration depth (PD), contrast resolution (CR), contrast sensitivity (CS), and generalized contrast-to-noise ratio (gCNR). Furthermore, a limited number of settings in CFI and CPWCI are used in those studies. In CFI, one focal depth is often only evaluated and compared to CPWCI, while different depths are of interest for different clinical applications. In CPWCI, multiple beamforming methods to reconstruct image lines (e.g., DAS or Fourier-based methods), number of steering angles, and angular combinations (e.g., 11 angles between $-11°$ and $11°$ or between $-5°$ and $5°$) might affect image quality.

Another limitation of the earlier mentioned studies is that the image quality was only evaluated in phantoms and not in human tissue. In US breast imaging, CPWCI can be an excellent candidate to replace CFI in automated breast volume scanners (ABVSs) or similar hybrid tomosynthesis-ultrasound scanners (HTUSs) [11] to decrease the relatively long scan times (60–90 s), which leads to breathing artifacts (especially in ABVS) and patient discomfort (by compression plates in HTUS). In ABVS and HTUS, a translating transducer collects US volumes of the whole breast facilitating US screening since volumes can be evaluated afterward. Thus, there is an urgent need to reduce scan times while preserving or improving image quality, which can be facilitated by CPWCI.

The aim was to evaluate whether CPWCI can result in at least similar image quality as CFI. Therefore, image quality parameters (gCNR, ResAx, ResLat, PD, CR, and CS) as defined in [9] and [12] were evaluated and compared between CPWCI using different steering angle combinations [Fig. 1(c)] and beamforming methods, and CFI at three focal depths [Fig. 1(a)]. US data were acquired in a dedicated phantom for image quality assurance using two transducers with different center frequencies (f_c) connected to a high-end US system, which is also used in clinical practice. In addition, we evaluated how the performance of CFI and CPWCI in terms of image quality translated into the clinical application breast imaging. To evaluate the performance of CFI and CPWCI in breast imaging, US images of a breast lesion were recorded by both methods in a similar to the phantom evaluation. Since incoherent compounding is commonly used in conventional breast US imaging, incoherent compounded US images were also recorded and evaluated. In incoherent compounding, US images of multiple steering angles are combined after postprocessing in contrast to coherent compounding in which RF or IQ data are combined.

II. Materials and Methods

A. Data Acquisition

Channel data (demodulated IQ-data) were recorded by a 14L5 and 10L4 transducer connected to a prototype Sequoia US system with research interface (Acuson Sequoia, Siemens Medical Solution, Mountain View, CA, USA) using CFI at three focal depths (d_f) and three steering angles (α: $-11°$, $0°$, and $11°$) and steered plane-wave acquisitions. The multipurpose phantom (model 040GSE, CIRS, Inc., Norfolk, VI, USA) used had an attenuation rate of 0.75 dB $\cdot$ cm^{-1} $\cdot$ MHz^{-1} similar to the rate of breast tissue [13]. The in-depth displaced wires, grayscale cysts (-9, -6, 0, 3, and 6 dB), vertical hypoechoic cysts, and homogenous part of the phantom were used to analyze Res, CR and CS, CNR, and PD, respectively. For PD, data were also recorded in air to capture electronic noise. Impulse response measurements (-6-dB cutoff) were used to determine the center frequency and the fractional bandwidth of the transmitted Gaussian pulses. The angles of the steered plane-wave acquisitions (α_i) were in the range $[-16°, 16°]$ ($[-0.28, 0.28]$ rad) and were calculated (in radians) according to

$$\alpha_i = \sin^{-1}(i\lambda/L), \quad i = -n_\alpha/2, \ldots, n_\alpha/2 - 1 \tag{1}$$

where L, λ, and n_α are the active array length of the transducer (38.4 mm), the wavelength of the pulse, and the total number of steered acquisitions, respectively [6]. The data acquisition settings are summarized in Table I.

As recommended by the European guidelines for quality assurance for US equipment [9], [10], all recordings were repeated five times in the same phantom but with targets (wires and cysts) at different lateral and elevational positions within the transducer's field-of-view (FOV) such that the speckle between the repeated images was fully decorrelated.

B. Image Reconstruction

Channel data acquired by plane-wave acquisitions were beamformed (two lines per pitch, same nonsteered grid for every α) by DAS [14], Stolt's-fk [5], and Lu's-fk [3], [4] algorithms. Data acquired by CFI were beamformed (two lines per pitch) by DAS using the hardware of the US system. Hamming apodization and dynamic focusing in receive (F-number; 10L4: 0.5, and 14L5: 0.8, based on element sensitivity) were

TABLE I
DATA ACQUISITION SETTINGS, INCLUDING FOCAL DEPTH (d_f), F-NUMBER (F#), SAMPLING (f_s) CENTER FREQUENCY (f_c), FRACTIONAL BANDWIDTH (F_{BW}), MECHANICAL INDEX (MI), AND ATTENUATED PULSE-INTENSITY INTEGRAL (P_{II3})

Trans*	d_f (mm)	F#	f_s (MHz)	f_c (MHz)†	F_{bw} (-)	MI (-)	P_{II3} (mJ·m^{-2})
10L4	10	3.6	11.4	6.4	0.65	1.2	0.0964
10L4	36	3.6	11.4	6.4	0.65	0.83	0.0593
10L4	62	3.6	11.4	6.4	0.65	0.79	0.0461
10L4	20000‡	0.0	11.4	6.4	0.65	0.68	0.0291
14L5	10	5.2	13.3	9.0	0.53	1.2	0.120
14L5	36	5.2	13.3	9.0	0.53	0.87	0.0361
14L5	62	5.2	13.3	9.0	0.53	0.80	0.0227
14L5	20000‡	0.0	13.3	9.0	0.53	0.77	0.0152

*Transducer; both have 192 elements and 38.4 lateral footprint.
†Demodulation frequency is equal to f_c in RF to IQ conversion.
‡Plane wave

applied in both software and hardware DAS algorithms. Angular weighting was applied in Stolt's-fk and Lu's-fk (angular range; 10L4: ±44°; and 14L5: ±32°) to achieve similar apodization as in DAS [15]. Beamformed plane-wave data were coherently compounded using the smallest angles around 0° calculated by (1) (narrow range, N) or as equally as possible distributed between −11° and 11° according to (1) (wide range, W). Next, power of the data was calculated, log-compressed to decibel scale, and then scan converted to a 100 μm × 100 μm imaging grid to reconstruct US power images for analysis. For visualization, the power images were converted into an 8-bit gray-level image with 60-dB dynamic range.

C. Image Quality Parameter Calculations

The quality of images by each acquisition and reconstruction type was evaluated as proposed by Thijssen *et al.* [9], Kollmann *et al.* [10], and Rodriguez-Molares *et al.* [12], although the power data instead of the final gray-level images were used in this study to prevent a dependency on the dynamic range.

1) Penetration Depth: PD is the maximal depth at which the image signal and noise become equal [16]. Therefore, the mean power was calculated for each depth using the reconstructed power data obtained in the homogenous part of the phantom (signal) and in air (electronic noise). The mean signal and noise were smoothed using a moving average filter (2 mm). The PD was defined as the depth at which the signal and noise power differed by less than 0.24 dB (i.e., dynamic resolution in an 8-bit US image with 60-dB dynamic range) for at least 0.5 mm.

2) Generalized Contrast-to-Noise Ratio: gCNR [12], which is robust against alterations in dynamic range by different beamformers, was used as a quantitative measure for the hypoechoic contrast at each imaging depth. First, the anechoic lesions were annotated. Second, for each annotated lesion, probability density functions were calculated for the power values in the area within 80% of the lesion radius and in the halo surrounding the lesion (inner and outer radius of 120 and 150%). Finally, the gCNR was calculated for each lesion

$$\mathrm{gCNR} = 1 - \mathrm{OVL} \tag{2}$$

where OVL is the overlap area between the two probability density functions.

3) Contrast Resolution: CR, sometimes referred to as gamma in the literature, is the number of gray levels to describe an increase of 1-dB contrast [9]. As CR depends on the dynamic range, the change of power (dB) of the beamformed signal to get an increase of 1 dB in contrast was used instead of gray levels in this study. Therefore, the grayscale disks were annotated similarly as for the quantification of gCNR. For each repeated measurement, CR was estimated from the slope between the mean power of each gray level disk and its contrast disk level (dB) using linear regression (least-squared error).

4) Contrast Sensitivity: CS is defined as the lesion signal-to-noise ratio (SNR_l) at 3-dB contrast [17]. First, the power values (dB) of each image that included a contrast disk were converted to linear contrast levels by dividing the power by the related CR and calculating the antilog. Next, the mean contrast level in each lesion (contrast disk) and background, including repeated measurements, was calculated (similar to gCNR). The SNR_L (or Mahalanobis distance) was calculated

$$\mathrm{SNR}_l = |\langle \mu_l \rangle \langle \mu_b \rangle| / \sqrt{\left(\sigma^2_{\mu l} + \sigma^2_{\mu b}\right)} \tag{3}$$

where $\langle \mu_l \rangle$ and $\langle \mu_b \rangle$ represent the assembly averages and $\langle \sigma^2_{\mu l} \rangle$ and $\langle \sigma^2_{\mu b} \rangle$ are the variances of the mean contrast level in each lesion with the same contrast (l) and its background (b) of the repeated measurements, respectively.

The SNR_l and its absolute contrast disk level were fitted to a linear model (least-squared error) to estimate the SNR_l at 3-dB contrast and its standard deviation [9].

5) Resolution: Res_{Ax} and Res_{Lat} were calculated based on the signals obtained from the wires orthogonal to the imaging plane. The positions of the wires were manually annotated and the full-width at half-maximum (FWHM) of the axial and lateral point-spread function (−6 dB) was calculated for each annotated wire using the reconstructed power data [18].

D. Statistical Analysis

For each image quality parameter and transducer, repeated measures ANOVA (SPSS Statistics 25, IBM, Armonk, NY, USA) was used to compare the means across the imaging methods based on the repeated observations. When significant ($p < 0.05$), marginal means were compared (Bonferroni confidence interval adjustment; p-value: 0.05). The methods CFI (d_f: 10, 36, and 62 mm) and CPWCI ($n_\alpha = 15$; wide and narrow angle range; and DAS, Stolt's-fk, and Lu's-fk) were compared.

E. Patient Measurement

The measurement protocol was approved by the local institutional ethical committee (CMO Radboudumc, project number CMO 2021-7421). In this study, data were acquired in one

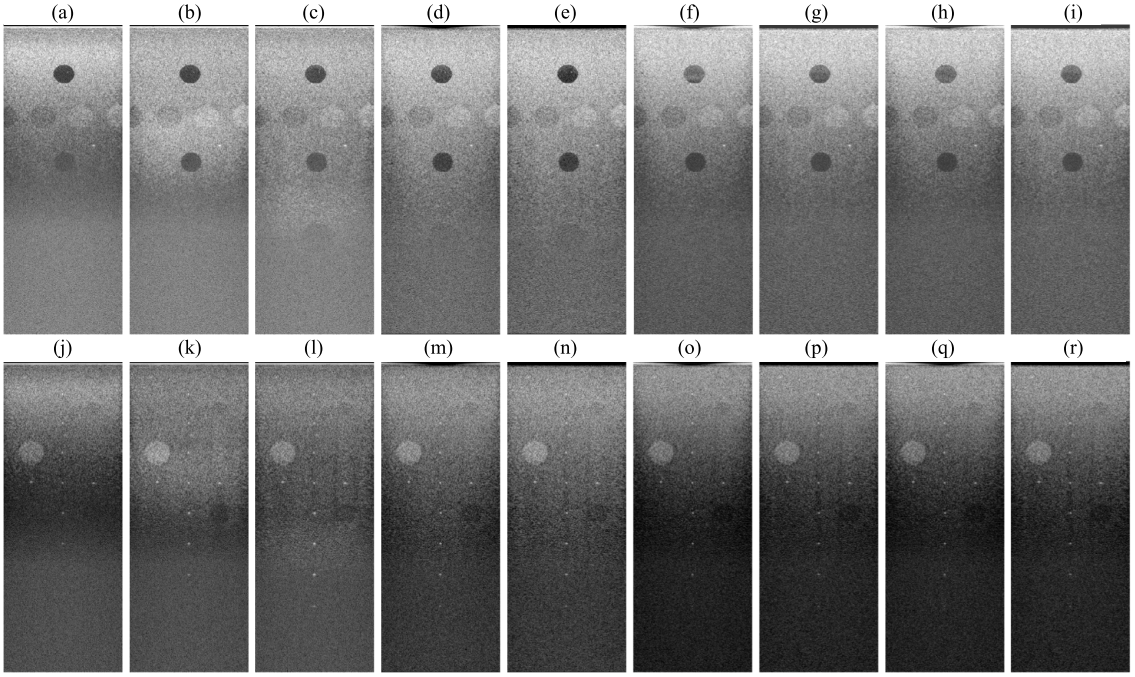

Fig. 2. B-mode images (38.4 mm × 100 mm; 60-dB dynamic range) by 14L5 of (a)–(i) hypoechoic cysts and wires (j)–(r) using CFI with focal depths at (a) and (j) 10, (b) and (k) 36, and (c) and (i) 62 mm and CPWCI reconstructed by (d), (e), (m), and (n) DAS, (f), (g), (o), and (p) Lu's-fk, and (h), (i), (q), and (r) Stolt's-fk and 15 steering angles (d), (f), (h), (m), (o), and (q) widely and (e), (g), (i), (n), (p), and (r) narrowly distributed.

patient with a palpable breast lesion (cyst). The patient gave written informed consent. The US data were acquired at the Radboud University Medical Center (Radboudumc, Nijmegen, The Netherlands) by an experienced radiologist. Images were reconstructed as described in Sections II-A and II-B. Next to the CFI (single angle) and CPWCI images, incoherent compounded images were reconstructed. In CFI, similar to in clinical systems, three images with different steering angles ($-11°$, $0°$, and $11°$) were combined after scan conversion. In CPWCI, three images were reconstructed by coherently compounding of three sets of five steering angles ([−13, −9], [−2, 2], and [9, 13]; steps of 1°) and also incoherently compounded. The images for the various acquisition sequences and beamforming methods were compared quantitatively.

III. Results

B-mode images of the hypoechoic cysts and wires acquired by all imaging methods can be seen in Figs. 2 and 3. The images of the cysts and wires were used to calculate the gCNR, and Res_{Ax} and Res_{Lat}, respectively. CR and CS were calculated by the contrast disks in the phantom (partly visible at 30 mm depth in Figs. 2(a)–(i) and 3(a)–(i) and PD by recordings in the homogenous part of the phantom and air. In this section, the results in terms of the aforementioned image quality parameters are described for each acquisition type (CFI and CPWCI) and transducer (14L5 and 10L4). For CPWCI, the effect of n_α, widely (W) and narrowly (N) distributed steering angles, and beamforming method (DAS, Stolt's-fk, and Lu-fk) is also presented.

A. Penetration Depth

Analyzing the 14L5 results, the PD of CPWCI (DAS) increased with n_α regardless of the angular distribution [Fig. 4(a)]. PD by CPWCI ($n_\alpha \geq 15$) ranged between 64 and 80 mm was significantly larger than CFI ($d_f = 36$ mm) and seemed almost independent of the applied beamforming method [Fig. 4(b)]. To reach a similar PD in CFI as CPWCI ($n_\alpha \geq 15$), d_f has to be increased to at least 36 mm. For the 10L4 [Fig. 4(c) and (d)], the PD was larger than 100 mm for all methods and n_α, except CFI ($d_f = 10$ mm), which had a PD of 97–100 mm.

B. Generalized Contrast-to-Noise Ratio

As visualized in Fig. 5(a), the average gCNR (all cysts above maximum PD) of CPWCI increased with n_α for the 14L5 and exceeded the gCNR of CFI ($d_f = 36$ mm) for $n_\alpha \geq 15$ for both W and N distributed angles. Analyzing the different beamforming methods and depths, the gCNR was similar for all methods at 16 mm depth except for Lu's-fk (W) and Stolt's-fk (W and N) methods in which the gCNR was minorly decreased compared to the CFI methods. At a depth of 44 mm, DAS (N) outperformed all CFI methods, whereas Stolt's-fk and Lu's-fk only outperformed CFI ($d_f = 10$ mm). At 68 mm, the gCNR was similar and close to zero for all methods except CFI ($d_f = 62$ mm) and DAS in which the gCNR was increased. Visual inspection of the B-mode images (Fig. 2) revealed that anechoic lesions could indeed still be noticed in CFI ($d_f = 62$ mm) and DAS, which was expected given the PD [Fig. 5(b)]. The gCNR seemed slightly increased comparing N and W distributed angles. The 10L4 transducer revealed similar results. The gCNR was similar to CFI ($d_f = 36$ mm) and CPWCI ($n_\alpha \geq 5$) for both W and N distributed angles [Fig. 5(c) and (d)] and all beamforming methods resulted in similar CNR at 17 and 45 mm except CFI ($d_f = 10$ mm). At 69 mm, CPWCI had an increased gCNR compared to CFI except for CFI ($d_f = 36$ mm) in which

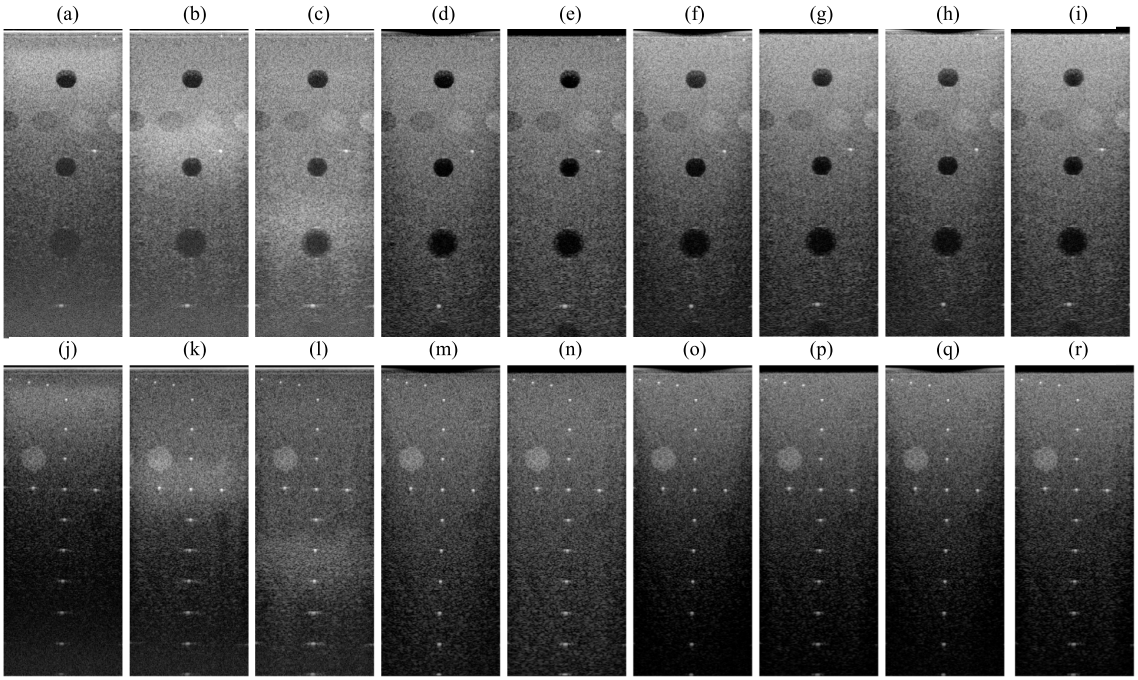

Fig. 3. B-mode images (38.4 mm × 100 mm; 60 dB dynamic range) by 10L4 of (a)–(i) hypoechoic cysts and (j)–(r) wires using CFI with focal depths at (a) and (j) 10, (b) and (k) 36, and (c) and (i) 62 mm and CPWCI reconstructed by (d), (e), (m), and (n) DAS, (f), (g), (o), and (p) Lu's-fk, and (h), (i), (q), and (r) Stolt's-fk and 15 steering angles (d), (f), (h), (m), (o), and (q) widely and (e), (g), (i), (n), (p), and (r) narrowly distributed.

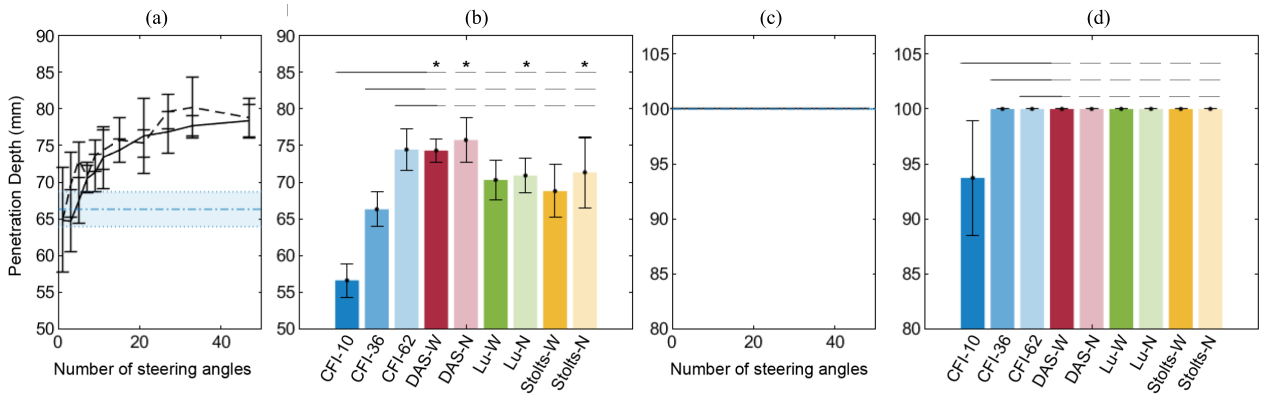

Fig. 4. Overview of the PD of all methods using (a) and (b) 14L5 and (c) and (d) 10L4 with (a) and (c) PD plotted against the number of steering angles (n_α) by CPWCI using DAS beamforming and widely (*W*, dashed line) or narrowly (*N*, solid line) distributed angles and the PD of CFI ($d_f = 36$ mm) visualized as a reference in blue and with (b) and (d) PD plotted for CFI ($d_f = 10$, 36, and 62 mm) and CPWCI ($n_\alpha = 15$; *W* and *N* distributed) and beamformed by DAS, Lu's-fk, and Stolt's-fk. The error bars in both graphs [and blue dotted lines in (a) and (c)] represent the mean PD and standard deviation by the five repeated measurements. The asterisk (*) indicates a significant difference ($p \leq 0.05$) in PD comparing all CFI and CPWCI methods; the statistical results of the three CFI methods compared to the CWPCI methods are only visualized.

gCNR was similar. The gCNR was slightly increased using *N* instead of *W* distributed angles, especially at lower depths.

C. Contrast Resolution

CR describes the increase in image intensity (power) when contrast increases by 1 dB. As can be seen in Fig. 6(a), CR increased with n_α from 1.08 to 1.25 in CPWCI ($n_\alpha \geq 7$) and was larger than CFI ($d_f = 10$). The differences between CPWCI methods [Fig. 6(b)] were minimally varying between 1.18 (Stolt's-fk-N) and 1.23 (DAS-N). For CFI ($d_f = 36$ mm), the contrast disks were in the focal spot (Fig. 2), which might explain the increased CR compared to the other CFI methods. Although CR differed between methods, the effect on the image quality would be nontrivial. Assuming an 8-bit image and 60-dB dynamic range, CR of 1.05 (CFI, $d_f = 10$) and 1.23 (DAS-N) would lead to 4.5 and 5.2 gray levels (rounded to 5), respectively, to describe 1-dB contrast. For the 10L4 transducer [Fig. 6(c) and (d)], CR was in the same range (1.10–1.27) for all methods. This range merely overlapped with the ranges found by the 14L5.

D. Contrast Sensitivity

CS is the lesion SNR_l at 3-dB contrast. The SNR_l was calculated similar to the CNR for hypoechoic lesions but using the antilog of the image power (see Section II) and thus is linearly related to the contrast level (in a decibel scale). The CS was independent of n_α in CPWCI [Fig. 7(a) and (c)] and most methods [Fig. 7(b) and (d)] for both transducers, except

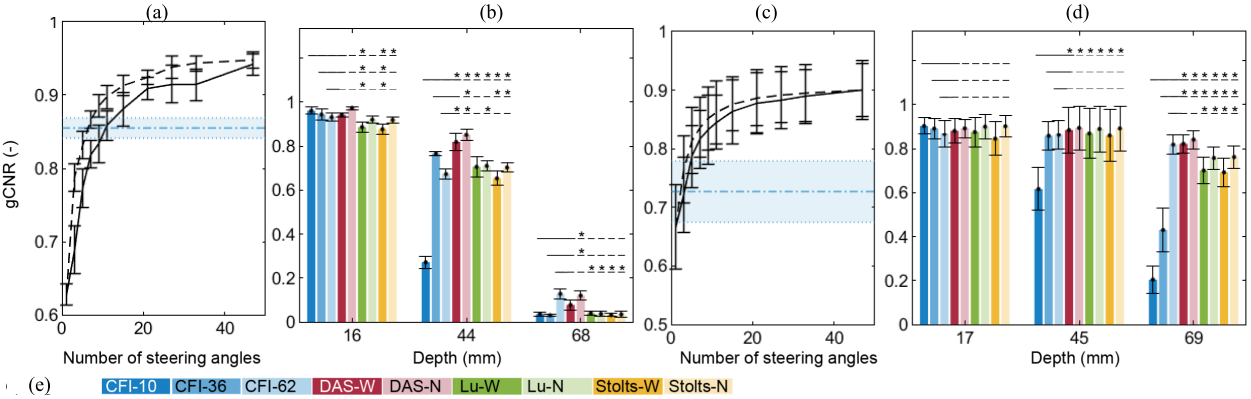

Fig. 5. Overview of the gCNR of all methods using (a) and (b) 14L5 and (c) and (d) 10L4 with (a) and (c) gCNR (14L5 average of lesion at 16 and 44 mm; 10L4 average of all three lesions within the PD) plotted against the number of steering angles (n_α) by CPWCI using DAS beamforming and widely (*W*, solid line) or narrowly (*N*, dashed line) distributed angles and the average CNR of CFI ($d_f = 36$ mm) visualized as a reference in blue and with (b) and (d) gCNR at three depths plotted for CFI ($d_f = 10$, 36, and 62 mm) and CPWCI ($n_\alpha = 15$; *W* and *N* distributed) beamformed by DAS, Lu's-fk, and Stolt's-fk. The error bars in both graphs [and blue dotted lines in (a) and (c)] represent the mean gCNR and standard deviation of the five repeated measurements and with (e) legend of (b) and (d). The asterisk (*) indicates a significant difference ($p \leq 0.05$) in gCNR comparing all CFI and CPWCI methods; the statistical results of the three CFI methods compared to the CWPCI methods are only visualized.

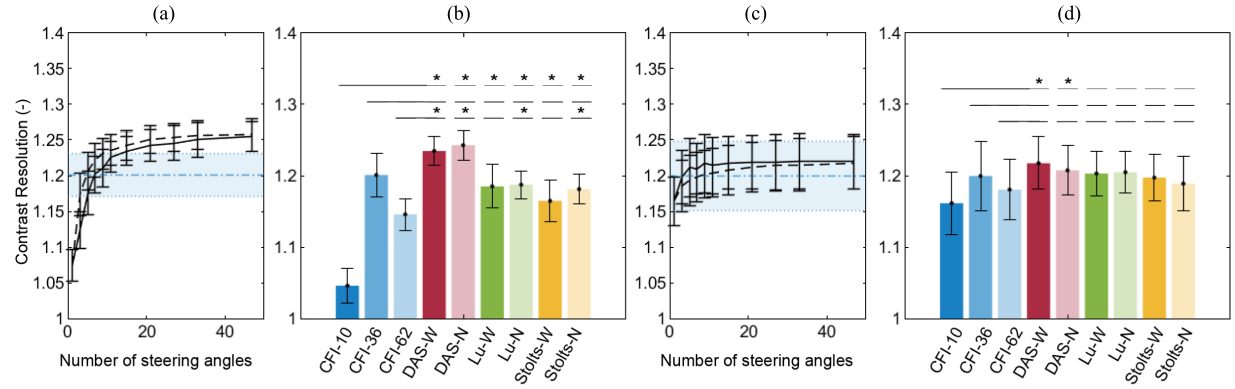

Fig. 6. Overview of the CR of all methods using (a) and (b) 14L5 and (c) and (d) 10L4 with (a) and (c) CR plotted against the number of steering angles (n_α) by CPWCI using DAS beamforming and widely (*W*, solid line) or narrowly (*N*, dashed line) distributed angles and the CR of CFI ($d_f = 36$ mm) visualized as a reference in blue and with (b) and (d) CR plotted for CFI ($d_f = 10$, 36, and 62 mm) and CPWCI ($n_\alpha = 15$; *W* and *N* distributed) and beamformed by DAS, Lu's-fk, and Stolt's-fk. The error bars in both graphs [blue dotted lines in (a) and (c)] represent the mean CR and standard deviation of the five repeated measurements. The asterisk (*) indicates a significant difference ($p \leq 0.05$) in CR comparing all CFI and CPWCI methods; the statistical results of the three CFI methods compared to the CWPCI methods are only visualized.

for Stolt's-fk and Lu's-fk beamforming in CPWCI for which CS was increased using narrowly distributed angles (14L5) and both distributions (10L4).

E. Axial Resolution

Res_{Ax} is expressed as the axial full-width-at-half-maximum (FWHM) of the phantom wires [Figs. 2(j)–(r) and 3(j)–(r)]. As can be observed in Fig. 8(a), the average FWHM in CPWCI was independent of n_α for 14L5. Almost all methods performed almost similarly at all depths [Fig. 8(b)]. As expected, FWHM decreased with imaging depth. For 10L4 [Fig. 8(c) and (d)], FWHM was similar for all depths except CFI at d_f of 62 mm, independent of n_α, and increased with depth. Res_{Ax} of the 10L4 was worse compared to that of the 14L5 as expected due to the longer transmitted wavelength.

F. Lateral Resolution

As can be observed in Fig. 9, Res_{Lat} was almost independent of n_α for both angular ranges in CPWCI for 14L5. In general, CPWCI using widely distributed angles resulted in improved Res_{Lat} compared to CFI outside the focal spot. In particular, Lu-fk performed better at all depths independently of the angular range. Lateral FWHM decreased with depth for all methods. Similar results can be noticed for the 10L4 transducer.

G. Patient Measurement

In Fig. 10, B-mode images of a cyst reconstructed by CFI and CPWCI are shown for both transducers. For CFI, images are shown at a focal depth of 10 and 36 mm in which the cyst was in and out of focus, respectively. DAS (*N*) and Lu's-fk (*W*) were visualized since those methods result in optimal gCNR and resolution, respectively. The images by CFI ($d_f = 10$ mm) and DAS (*N*) seemed to result in similar image quality by visual inspection. As expected, the contrast in Lu's-fk (*W*) was reduced compared to DAS (*N*) and CFI ($d_f = 10$ mm). However, the resolution seemed to be improved by inspecting the speckle and small (dot shaped) structures. The image quality of CFI (df 36 mm) was inferior as the lesion was out of focus.

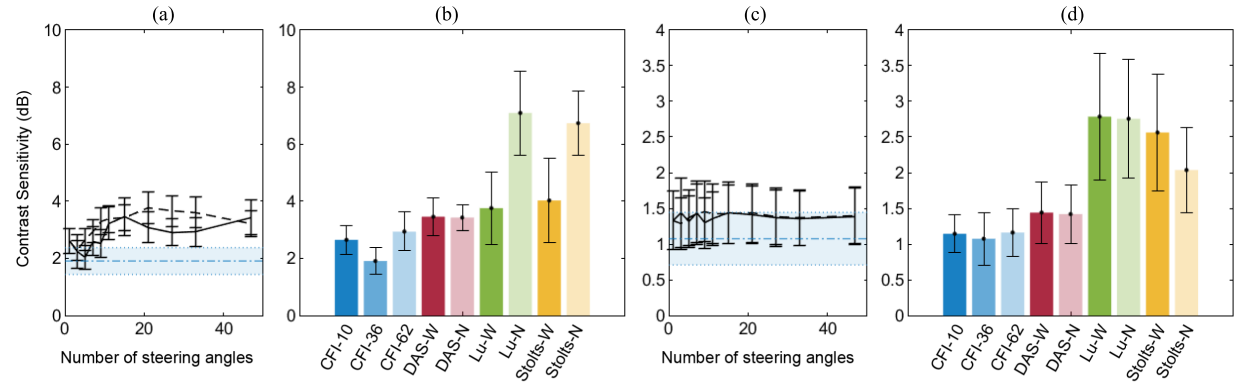

Fig. 7. Overview of the CS of all methods using (a) and (b) 14L5 and (c) and (d) 10L4 with (a) and (c) CS plotted against the number of steering angles (n_α) by CPWCI using DAS beamforming and widely (*W*, solid line) or narrowly (*N*, dashed line) distributed angles and the CS of CFI ($d_f = 36$ mm) visualized as a reference in blue and with (b) and (d) CS plotted for CFI ($d_f = 10$, 36, and 62 mm) and CPWCI ($n_\alpha = 15$; *W* and *N* distributed) and beamformed by DAS, Lu's-fk, and Stolt's-fk. The error bars in both graphs [blue dotted lines in (a) and (c)] represent the mean and standard deviation of the linear fit. Since the five repeated measurements were required for the linear fit to estimate CS, repeated measures ANOVA could not be applied for CS to compare means.

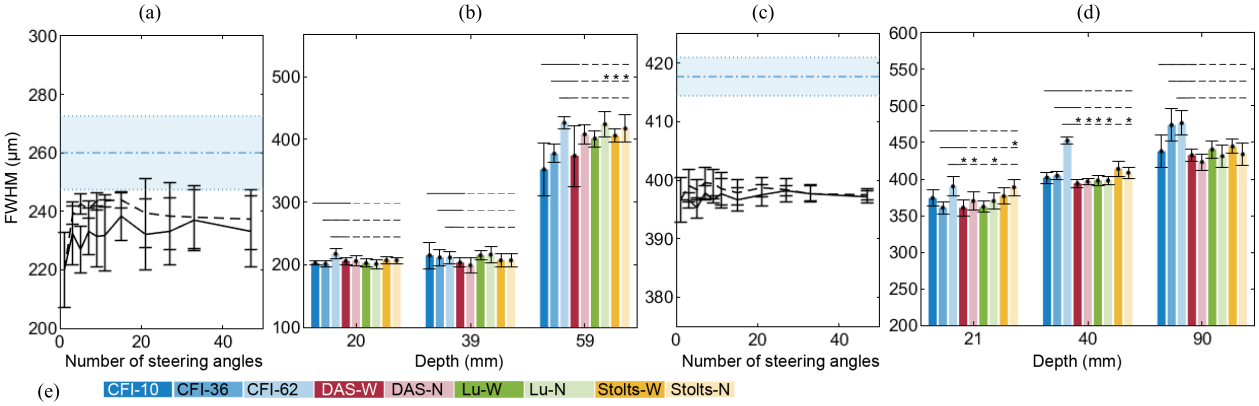

Fig. 8. Overview of the axial resolution (Res_{Ax}) of all methods using (a) and (b) 14L5 and (c) and (d) 10L4 with (a) and (c) average axial FWHM (14L5: 0–60 and 10L4: 0–90 mm depth) plotted against the number of steering angles (n_α) by CPWCI using DAS beamforming and widely (*W*, solid line) or narrowly (*N*, dashed line) distributed angles and the FWHM of CFI ($d_f = 36$ mm) visualized as a reference in blue, respectively; with (b) and (d) FWHM at three depths plotted for CFI ($d_f = 10$, 36, and 62 mm) and CPWCI ($n_\alpha = 15$; *W* and *N* distributed) beamformed by DAS, Lu'-fk, and Stolt's-fk. The error bars in both graphs [blue dotted lines in (a) and (c)] represent the mean FWHM and standard deviation of the five repeated measurements and with (e) legend of (b) and (d). The asterisk (*) indicates a significant difference ($p \leq 0.05$) in Res_{Ax} comparing all CFI and CPWCI methods; the statistical results of the three CFI methods compared to the CWPCI methods are only visualized.

Since incoherent compounding is often applied in conventional breast imaging, the B-mode images by that approach were also compared. As can be seen in Fig. 10, the incoherent compounded images seemed similar between CFI and CPWCI (DAS-N) for both transducers.

IV. Discussion

For the 14L5 transducer, a typical transducer used in breast imaging (e.g., in ABVS), we showed that CPWCI (14L5, $n_\alpha \geq 15$) resulted in similar image quality to CFI and even improved quality at increased depths. Compared to CFI, CPWCI ($n_\alpha \geq 15$) had an improved PD, gCNR (at lower depths) and Res_{Lat}, and similar Res_{Ax}, gCNR, CR, and CS. The choice of beamforming method and angular distribution type in CPWCI can improve specific image quality parameters: gCNR by DAS and narrowly distributed angles; CS by Lu's-fk or Stolt's-fk and narrowly distributed angles; and Res_{Lat} by Lu's-fk and widely distributed angles. These results were backed up by comparing CFI and CPWCI in a clinical case (Figs. 10 and 11). Summarizing, CPWCI ($n_\alpha \geq 15$) had an improved frame rate, up to 38× in case of incoherent compounding, compared to CFI while preserving image quality and improving PD. It is expected that CPWCI will lead to further improved image quality when used for volumetric imaging (e.g., ABVS) as CPWCI dramatically reduces scan times, and thus, the volumetric images will be deteriorated less by breathing artifacts.

For the 10L4 transducer, similar results were found in comparing CFI and CPWCI. In general, this transducer benefitted from an improved PD [>100 mm, Fig. 4(c) and (d)] compared to 14L5 [53–80 mm, Fig. 4(a) and (b)] at cost of resolution. Switching from 14L5 with CFI to 10L4 with CPWCI ($n_\alpha = 15$) resulted in an increased PD, improved gCNR at increased depths (>30 mm) (Fig. 5), and similar CR (Fig. 6), however, at cost of CS (factor 1.2×–2.4×, see Fig. 7) and Res_{Lat} (397–484 μm, average at ≤60 mm depth, and CFI ($d_f = 36$ mm) compared to DAS-W, see Fig. 9).

In CPWCI, image quality parameters can be tuned by the choice of angular distribution or beamforming method (e.g., CS by choosing Stolt's-fk or Lu's-fk, res_{lat} by Lu's-fk,

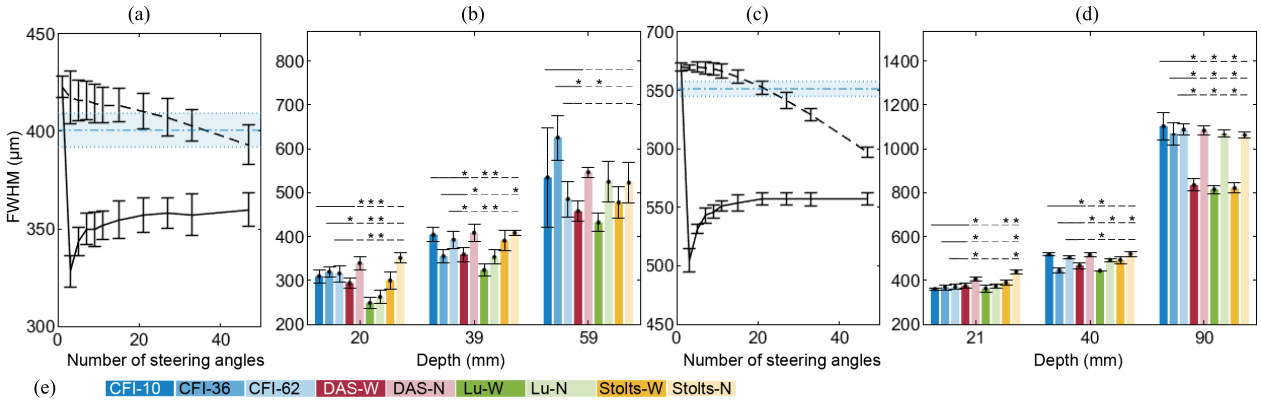

Fig. 9. Overview of the lateral resolution (Res_{Lat}) of all methods using (a) and (b) 14L5 and (c) and (d) 10L4 with (a) and (c) lateral FWHM (14L5: 0–60 and 10L4: 0–90 mm depth) plotted against the number of steering angles (n_α) by CPWCI using DAS beamforming and widely (*W*, solid line) or narrowly (*N*, dashed line) distributed angles and the FWHM of CFI ($d_f = 36$ mm) visualized as a reference in blue; with (b) and (d) FWHM at three depths plotted for CFI ($d_f = 10$, 36, and 62 mm) and CPWCI ($n_\alpha = 15$; *W* and *N* distributed) beamformed by DAS, Lu's-fk, and Stolt's-fk. The error bars in both graphs [blue dotted lines in (a) and (c)] represent the mean FWHM and standard deviation of the five repeated measurements and with (e) legend of (b) and (d). The asterisk (*) indicates a significant difference ($p \leq 0.05$) in Res_{Lat} comparing all CFI and CPWCI methods; the statistical results of the three CFI methods compared to the CWPCI methods are only visualized.

and gCNR by narrow distribution), and however, this may affect other parameters. A reader study in women with breast lesions is required to investigate if those changes in image quality by switching transducers will be beneficial in breast cancer detection.

It is clear that PD was improved by all CPWCI methods but was limited for CFI using 14L5. In CFI, the transmitted energy is concentrated in the focus, and reduced energy is present at depths behind d_f, thus limiting PD. This can be noticed by the increased PD when the focal depth was increased [Fig. 4(b)]. In PWI, energy is per definition more equally distributed due to the lack of a focal spot, which resulted in reduced energy throughout the imaging plane. This energy reduction was compensated by compounding sufficient steering angles in CPWCI. Consequently, PD was increased and image quality was similar or even improved throughout the entire imaging plane compared to CFI, which had the best image quality around the focal spot and can be seen comparing CFI and CPWCI in the *in vivo* case (Fig. 10). Because of the lower f_c, the PD using 10L4 was more than 100 mm for almost all methods except for CFI with focal depth at 10 mm.

The gCNR at shallow depths (∼16 mm) was similar for CFI and all CPWCI ($n_\alpha \geq 15$) methods [Fig. 5(b)] for 14L5. At intermediate depths (∼44 mm), CFI (d_f at intermediate or low depths) and CPWCI had similar contrast and DAS (*N*) even outperformed CFI. In CPWCI, gCNR can be improved by using narrowly instead of widely distributed angles [Fig. 5(b) and (d)] or by increasing the F-number in DAS or decreasing the angular filter range in the fk-methods. The slightly reduced gCNR for wide compared to narrow angular distribution can be explained by the reduction of element sensitivity, thus decreasing SNR for increasing steering angles used in compounding. In all approaches, the contribution for signals received from large angles, and thus of signals with reduced signal-to-noise ratios due to element directivity reducing the CNR, is limited. For 10L4, CPWCI had improved gCNR at large depths (69 mm) and all methods performed similarly above 60 mm except for CFI ($d_f = 10$ mm) because of the relatively shallow focus.

Although the fk-methods had slightly reduced gCNR compared to DAS, the CS was improved. This means that those methods were more sensitive for small changes in contrast, i.e., higher SNR_l at 3-dB contrast but were performing less in hypoechoic areas. As discussed before, gCNR in fk-methods might be improved by using narrowly distributed angles or decreasing the angular filter range. It is expected that the CS will then also improve as the CS in fk-methods was only improved using a narrow distribution for the 14L5. CS may be related to the beamforming methods since both CFI (DAS on hardware) and CPWCI using DAS had similar CS, whereas CS using fk-methods was improved (Fig. 7). A CR seemed method independent as it hardly differed between methods. It might be mainly related to the transmit power of the system, which was assumed to be equal for all methods and transducers.

Compared to CFI, Res_{Lat} was improved in CPWCI using widely distributed angles independently of n_α, beamforming method, or transducer, especially at lower depths (>50 mm). This improvement in resolution compared to CFI and CPWCI (N) can be explained by the insonification of large, widely distributed steering angles (±11°). Lu's-fk resulted in an improved Res_{Lat} compared to DAS, which may be related to the derivation of Lu's-fk, which is based on the full-wave modeling of the acoustic wave propagation. With a more comprehensive modeling manner, Lu's-fk is probably able to produce a better spatial resolution than DAS. Res_{Ax} seemed independent of methods (CPWCI and CFI) although CPWCI seemed to perform better around the maximal PD [Fig. 8(b) and (d)]. Both Res_{Ax} and Res_{Lat} were dependent on the transducer chosen (Figs. 8 and 9), which can be explained by the increased wavelength comparing 14L5 ($f_c = 9.0$ MHz) and 10L4 ($fc = 6.4$ MHz).

The above results were supported by the *in vivo* case in which B-mode images of a cyst by CPWCI and CFI

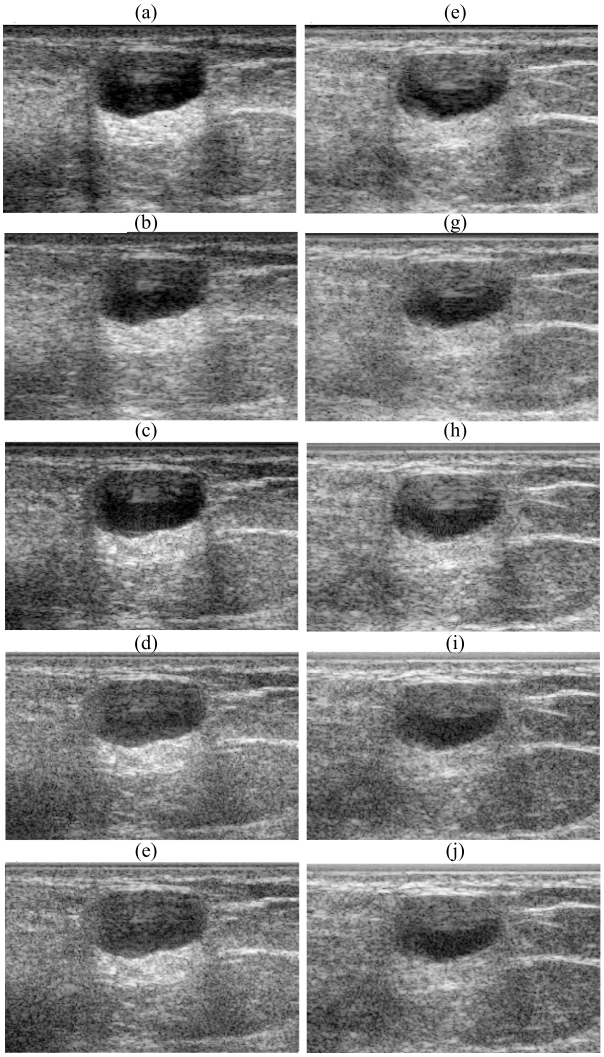

Fig. 10. B-mode images (dynamic range 60 dB, 32 mm × 20 mm) of a cyst obtained by (a)–(e) 14L5 and (f)–(j) 10L4, and reconstructed by CFI with focal depth at (a) and (f) 10 and (b) and (g) 36 mm; CPWCI with DAS using (c) and (h) narrowly and (d) and (i) Lu's-fk and (e) and (j) Stolt's-fk using widely distributed angles.

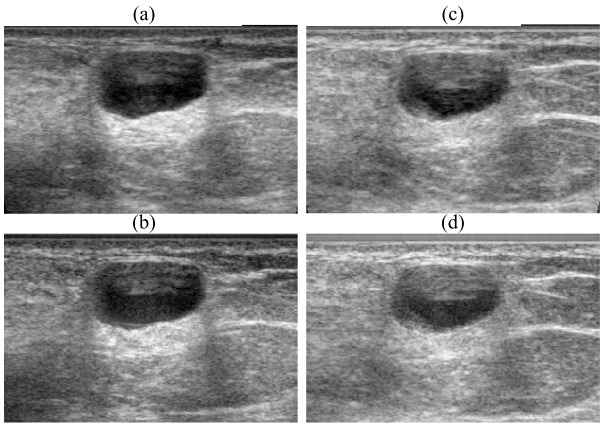

Fig. 11. Incoherently compounded B-mode images (dynamic range 60 dB, 32 mm × 20 mm) of a cyst obtained by 14L5 (a) and (b) 14L5 and (c) and (d) 10L4, and reconstructed by CFI with focal depth at (a) and (c) 10 mm and (b) and (d) CPWCI with DAS using narrowly distributed angles.

were obtained (Figs. 10 and 11). The images by CFI ($df = 10$ mm) and CPWCI (DAS-N) seemed similar on visual inspection, which was expected since the phantom results revealed similar resolution and gCNR. The reduced gCNR and improved Res_{lat} in Lu's-fk compared to DAS (N) can also be clearly noticed by the reduced contrast of the cyst, and smaller speckle and sharper structures, respectively. Those similar findings in phantom and *in vivo* results were not trivial beforehand. The speed of sound of the used phantom was homogenous (1540 m · s^{-1}), whereas it can vary in breast between 1422 (fat) and 1487 (breast parenchyma) and can be even over 1548 m · s^{-1} in breast cancers [19]. Especially in CPWCI, differences in speed of sound may introduce artifacts because of misalignments US data by different steering angles in coherent compounding. However, those artifacts were not noticed in the *in vivo* case.

CPWCI has high protentional to replace CFI in breast imaging, especially in volumetric breast scanners (e.g., ABVS and HTUS) in which 2-D images are obtained and processed frame-by-frame. By implementing CPWCI ($n_\alpha = 15$), the scan time can be reduced by a factor 13 and even 38 compared to CFI by single angle and incoherent compounding, respectively, in 192 channel system (e.g., ABVS). The image quality will be preserved after implementation of CWPCI given the phantom and the *in vivo* results in this study. It is even expected that the image quality will increase by CPWCI as the scan time can be reduced to less than 5 s and breathing artifacts will be avoided. Another benefit of CPWCI is that image quality is not dependent on the focal depth as it is in CFI, which can be seen in comparing the two focal depths in Fig. 10. Therefore, CPWCI is especially beneficial to ABVS since the lesion depth is unknown beforehand. The elevational transducer translation in ABVS was not evaluated in this study; however, Holländer *et al.* [8] showed that translation speed did not affect image quality up to a depth of 50 mm and speed of 50 mm · s^{-1} (3-s scan time in ABVS). It is expected that the image quality at larger depths will also not be affected because of the increasing elevational beamwidth (slice thickness) at lower depths.

To replace CFI by CPWCI, it is recommended to use wider distributed angles since the small decrease in contrast is compensated by a highly improved lateral resolution, which is an important consideration to distinguish details in clinical practice. Furthermore, large steering angles can reduce shadowing artifacts by a wide-angle insonification beneath the nipple or other wave-blocking structures. A trapezoidal field-of-view (FOV) instead of a rectangular under the transducer can also be reconstructed using large angles, and thus, breast tissue close to the chest wall can be imaged in HTUS.

In breast imaging but also in general, it is advised to use Lu's-fk or DAS beamforming to focus on resolution or contrast, respectively. The advantage of DAS is that reconstruction can be performed on the system hardware, whereas the fk-methods require powerful processing power (e.g., GPU) for software reconstruction. If software reconstruction is required, fk-methods may be beneficial given their smaller computational complexity compared to DAS. Lu's-fk can be advised to partly limit the loss in resolution when switching to lower

f_c to improve PD. f_c can be lowered by switching transducers (e.g., 14L5–10L4) or by increasing the wavelength of the transmitted pulse that is limited by the bandwidth of the transducer.

To solely compare the effect of the acquisition and beamforming methods, postprocessing (e.g., speckle reduction and contrast enhancement) was not applied mainly because postprocessing is user and vendor dependent. Some postprocessing steps may further improve the image quality and might be required for an *in vivo* reader study, which will be the next step. Clinicians are interested in, and used to, the final processed images and are not used to evaluate nonprocessed images that are often not optimized for visualization. Therefore, the next step will be a reader study, including image postprocessing to investigate whether CPWCI can replace CFI. In addition, it can be investigated, in which tradeoff between resolution and contrast is optimal in a similar study. Although we compared CPWCI and CFI in an *in vivo* case, an extended *in vivo* study is interesting to investigate further what the effect is of different lesion types, speed-of-sound differences between tissues, shadowing, and other *in vivo*-related artifacts.

V. Conclusion

In this study, we showed on a clinical high-end system that the image quality was similar or even improved when applying CPWCI ($n_\alpha = 15$) compared to CFI. Above 45 mm depth, the CS, CR, Res_{Ax}, and gCNR were found similar, while the PD and Res_{Lat} improved as well as the gCNR (below 45 mm). In CPWCI, the distribution of angles and beamforming method can be used to improve contrast (narrowly distributed angles, DAS) or resolution (widely distributed angles Lu's-fk). These results were corroborated by comparing CFI and CPWCI in a clinical case (i.e., cyst in breast imaging). To conclude, CPWCI is showing increased PD and Res_{Lat} quality metrics, and increased frame rates (up to 38×) compared to CFI.

References

[1] B. Delannoy, R. Torguet, C. Bruneel, and E. Bridoux, "Ultrafast electronical image reconstruction device," in *Echocardiology*, C. T. Lancée, Ed. Dordrecht, The Netherlands: Springer, 1979, pp. 447–450.

[2] B. Delannoy, R. Torguet, C. Bruneel, E. Bridoux, J. M. Rouvaen, and H. Lasota, "Acoustical image reconstruction in parallel-processing analog electronic systems," *J. Appl. Phys.*, vol. 50, no. 5, pp. 3153–3159, 1979.

[3] J.-Y. Lu, "2D and 3D high frame rate imaging with limited diffraction beams," *IEEE Trans. Ultrason., Ferroelectr., Freq. Control*, vol. 44, no. 4, pp. 839–856, Jul. 1997.

[4] J.-Y. Lu, "Experimental study of high frame rate imaging with limited diffraction beams," *IEEE Trans. Ultrason., Ferroelectr., Freq. Control*, vol. 45, no. 1, pp. 84–97, Jan. 1998.

[5] D. Garcia, L. Le Tarnec, S. Muth, E. Montagnon, J. Poree, and G. Cloutier, "Stolt's f-k migration for plane wave ultrasound imaging," *IEEE Trans. Ultrason., Ferroelectr., Freq. Control*, vol. 60, no. 9, pp. 1853–1867, Sep. 2013.

[6] G. Montaldo, M. Tanter, J. Bercoff, N. Benech, and M. Fink, "Coherent plane-wave compounding for very high frame rate ultrasonography and transient elastography," *IEEE Trans. Ultrason., Ferroelectr., Freq. Control*, vol. 56, no. 3, pp. 489–506, Mar. 2009.

[7] T.-K. Song and J. H. Chang, "Synthetic aperture focusing method for ultrasound imaging based on planar waves," *J. Acoust. Soc. Amer.*, vol. 116, p. 1884, Jan. 2004.

[8] B. Holländer, G. A. G. M. Hendriks, R. M. Mann, H. H. G. Hansen, and C. L. de Korte, "Plane-wave compounding in automated breast volume scanning: A phantom-based study," *Ultrasound Med. Biol.*, vol. 42, no. 10, pp. 2493–2503, Jan. 2016.

[9] J. M. Thijssen, G. Weijers, and C. L. de Korte, "Objective performance testing and quality assurance of medical ultrasound equipment," *Ultrasound Med. Biol.*, vol. 33, no. 3, pp. 460–471, Mar. 2007.

[10] C. Kollmann *et al.*, "Guideline for technical quality assurance (TQA) of ultrasound devices (B-mode)–version 1.0 (July 2012)," *Ultraschall der Medizin-Eur. J. Ultrasound*, vol. 33, no. 6, pp. 544–549, Dec. 2012.

[11] B. Schaefgen *et al.*, "Initial results of the FUSION-X-U.S. prototype combining 3D automated breast ultrasound and digital breast tomosynthesis," *Eur. Radiol.*, vol. 28, no. 6, pp. 2499–2506, Jun. 2018.

[12] A. Rodriguez-Molares *et al.*, "The generalized contrast-to-noise ratio: A formal definition for lesion detectability," *IEEE Trans. Ultrason., Ferroelectr., Freq. Control*, vol. 67, no. 4, pp. 745–759, Apr. 2019.

[13] H. G. Nasief, I. M. Rosado-Mendez, J. A. Zagzebski, and T. J. Hall, "Acoustic properties of breast fat," *J. Ultrasound Med.*, vol. 34, no. 11, pp. 2007–2016, Nov. 2015.

[14] D. C. M. Horvat, J. S. Bird, and M. M. Goulding, "True time-delay bandpass beamforming," *IEEE J. Ocean. Eng.*, vol. 17, no. 2, pp. 185–192, Apr. 1992.

[15] C. Chen, G. A. G. M. Hendriks, R. J. G. van Sloun, H. H. G. Hansen, and C. L. de Korte, "Improved plane-wave ultrasound beamforming by incorporating angular weighting and coherent compounding in Fourier domain," *IEEE Trans. Ultrason., Ferroelectr., Freq. Control*, vol. 65, no. 5, pp. 749–765, May 2018.

[16] K. R. Gorny, D. J. Tradup, and N. J. Hangiandreou, "Implementation and validation of three automated methods for measuring ultrasound maximum depth of penetration: Application to ultrasound quality control," *Med. Phys.*, vol. 32, no. 8, pp. 2615–2628, Aug. 2005.

[17] J. M. Thijssen, M. C. van Wijk, and M. H. M. Cuypers, "Performance testing of medical echo/Doppler equipment," *Eur. J. Ultrasound*, vol. 15, no. 3, pp. 151–164, Oct. 2002.

[18] H. Liebgott, A. Rodriguez-Molares, F. Cervenansky, J. A. Jensen, and O. Bernard, "Plane-wave imaging challenge in medical ultrasound," in *Proc. IEEE Int. Ultrason. Symp. (IUS)*, Sep. 2016, pp. 1–4.

[19] C. Li, N. Duric, P. Littrup, and L. Huang, "*In vivo* breast sound-speed imaging with ultrasound tomography," *Ultrasound Med. Biol.*, vol. 35, no. 10, pp. 1615–1628, Oct. 2009.

Gijs A. G. M. Hendriks (Member, IEEE) received the B.Sc. and M.Sc. degrees in biomedical engineering from the Eindhoven University of Technology, Eindhoven, The Netherlands, in 2011 and 2014, respectively, and the Ph.D. degree in medical ultrasound imaging from the Radboud University Medical Center, Nijmegen, The Netherlands, in 2019.

As part of his Ph.D. program, he focused on the implementation of 3-D elastography and ultrafast ultrasound imaging techniques on an automated breast volume scanner to improve the specificity of diagnosing malignant breast lesions. Since 2018, he has been working as a Postdoctoral Researcher on integration of 3-D ultrasound and tomosynthesis in a new device at the Radboud University Medical Center.

Gert Weijers studied electrical engineering at the Saxion Hogeschool, Enschede, The Netherlands.

In 2004, he joined the Clinical Physics Laboratory, Department of Pediatrics, Radboud University Medical Center, Nijmegen, The Netherlands. He is currently a Researcher with the Department of Radiology, Radboud University Medical Center. His special research interests are quality assurance for ultrasound equipment, for which he developed the QA4US software package, cardiac 2-D strain analysis for which he developed postprocessing software and a research platform, and quantitative ultrasound imaging for staging the hepatic fat content. The latter was also the topic for his Ph.D. project, which resulted in the thesis entitled "Staging Liver Fat by Quantitative Ultrasound" in 2019. In 2018, he received the NWO OpenMind Grant for his research on fetal lung maturity classification using similar ultrasound methodology as developed during his Ph.D. degree. Currently, he is investigating and comparing various ultrasound methods for staging hepatic steatosis and fibrosis in large clinical studies.

Chuan Chen (Student Member, IEEE) received the Ph.D. degree in medical science from the Radboud University Medical Center, Nijmegen, The Netherlands, in 2021.

Currently, he works as a Postdoctoral Researcher at the Eindhoven University of Technology, Eindhoven, The Netherlands. His main field of work is the development of medical ultrasound techniques, including ultrasound image reconstruction and contrast-enhanced ultrasound.

Madeleine Hertel (Student Member, IEEE) was born in Nuremberg, Germany, in 1992. She received the master's degree in physics from the Karlsruhe Institute of Technology (KIT), Karlsruhe, Germany, in 2017. She is currently pursuing the Ph.D. degree with Siemens Healthcare, Forchheim, Germany, in cooperation with Prof. Dr. Georg Rose at the Institute of Medical Engineering, Research Campus STIMULATE, Otto-von-Guericke-University, Magdeburg, Germany.

Her main field of research is breast imaging focused on the compression behavior in mammographic imaging modalities.

Ms. Hertel has been a Student Member of the IEEE UFFC Society since 2019 and a member of the IEEE UFFC-S Industry Engagement Committee. She was the IEEE UFFC-S Senior Student Representative for Ultrasonics from 2020 to 2021.

Chi-Yin Lee (Senior Member, IEEE) received the B.Sc. degree in electronics from The Chinese University of Hong Kong, Hong Kong, in 1987, and the M.Sc. degree in electrical engineering, the M.Sc. degree in applied mathematics, and the Ph.D. degree in electrical engineering from Brown University, Providence, RI, USA, in 1989, 1991, and 1993, respectively.

From 1993 to 1998, he was an Advanced Development Engineer with the MRI and Image Guided Surgery Division, Picker International (now Philips Healthcare), Highland Heights, OH, USA. He joined the Ultrasound Division, Siemens Medical Solutions, Issaquah, WA, USA, in 1998, as a Staff Software Engineer. He is currently a Principal Systems Engineer with the Advanced Applications Group.

Peter M. Dueppenbecker received the Dipl.Ing. degree in electrical engineering and information technology from RWTH Aachen University, Aachen, Germany, in 2010, and the Ph.D. degree in imaging sciences and biomedical engineering from King's College London, London, U.K., in 2016.

He currently works as a Senior Key Expert for multimodality imaging systems and the Predevelopment Team Lead at Siemens Healthineers, Erlangen, Germany.

Marcus Radicke was born in Wesel, Germany, in 1982. He studied physics at the University of Bonn, Bonn, Germany, and Milan, Italy. He received the Diploma degree and the Ph.D. degree, with a thesis on acoustic radiation contrast in MR phase images—a method to visualize changes in elasticity, ultrasonic loss, and sound impedance, from the University of Bonn, Bonn, Germany, in 2007 and 2009, respectively.

In 2010, he held a postdoctoral position at the University of Bonn until he started working at the Diagnostic Imaging Section, Innovation Department of X-Ray Products, Siemens Healthcare, as a Research Scientist. In 2016, he became a Senior Key Expert in for X-ray physics and is in charge of the physics-related topics within the development of future breast imaging platforms at the business unit X-ray products.

Hendrik H. G. Hansen received the M.Sc. degree in applied physics from the Eindhoven University of Technology, Eindhoven, The Netherlands, in 2005, and the Ph.D. degree from Radboud University, Nijmegen, The Netherlands in 2012, with a focus on noninvasive vascular ultrasound strain elastography for vulnerable plaque detection in carotid arteries.

After graduation, he briefly worked as a Software/System Test Engineer at Assembléon BV, Veldhoven, The Netherlands. Since 2007, he has been with the Medical UltraSound Imaging Center (MUSIC), Radboud University Medical Center, Nijmegen, The Netherlands. In the years after, he worked on developing ultrafast functional ultrasound techniques, such as 3-D strain elastography, 3-D blood flow imaging, and shear wave elastography (SWE) for vascular applications and breast cancer detection. In November 2017, he obtained a permanent position with MUSIC, where he was appointed as Assistant Professor in 2020. He is currently leading a research group on shear wave imaging, which aims at further advancement of quantitative elastography technology such as shear wave elastography (SWE) and translation of this technology to clinic for a variety of applications. He has (co)authored over 40 peer-reviewed scientific articles and book chapters.

Dr. Hansen is a member of the International IEC Committee and the United States FDA-committee working on guidelines for SWE application in liver. Four Ph.D. students already graduated under his supervision and four more are currently under his supervision.

Chris L. de Korte (Senior Member, IEEE) received the M.Sc. degree in electrical engineering from the Eindhoven University of Technology, Eindhoven, The Netherlands, in 1993, and the Ph.D. degree in medical sciences from the Thoraxcenter, Erasmus University Rotterdam, Rotterdam, The Netherlands, in 1999, with a focus on intravascular ultrasound elastography.

In 2002, he joined the Clinical Physics Laboratory, Radboud University Medical Center, Nijmegen, The Netherlands, as an Assistant Professor, where he became the Head in 2004. In 2006, he was an Associate Professor of medical ultrasound techniques and he finished his training as a Medical Physicist in 2007. Since 2012, he has been the Founder and the Director of the Medical UltraSound Imaging Center (MUSIV), Department of Medical Imaging, Radboud University Medical Center (Radboudumc), Nijmegen, The Netherlands. He was appointed as a Full Professor on medical ultrasound techniques in 2015. Since 2016, he has been a Full Professor of medical ultrasound imaging with the University of Twente, Enschede, The Netherlands. He has (co)authored over 200 peer-reviewed articles in international journals and is (co)inventor of four patents. His research interests include functional imaging and acoustical tissue characterization for diagnosis, treatment monitoring, and guiding interventions for oncology and vascular applications. Recently, he also focuses on artificial intelligence-driven apps for point-of-care ultrasound.

Dr. de Korte was a recipient of the EUROSON Young Investigator Award of the European Federation of Societies for Ultrasound in Medicine and Biology in 1998.